
This item was submitted to [Loughborough's Research Repository](#) by the author.
Items in Figshare are protected by copyright, with all rights reserved, unless otherwise indicated.

Single-walled carbon nanotubes enhance the efficiency and stability of mesoscopic perovskite solar cells

PLEASE CITE THE PUBLISHED VERSION

<http://dx.doi.org/10.1021/acsami.7b04894>

PUBLISHER

© American Chemical Society

VERSION

AM (Accepted Manuscript)

PUBLISHER STATEMENT

This work is made available according to the conditions of the Creative Commons Attribution-NonCommercial-NoDerivatives 4.0 International (CC BY-NC-ND 4.0) licence. Full details of this licence are available at: <https://creativecommons.org/licenses/by-nc-nd/4.0/>

LICENCE

CC BY-NC-ND 4.0

REPOSITORY RECORD

Batmunkh, Munkhbayar, C.J. Shearer, Munkhjargal Bat-Erdene, Mark J. Biggs, and J.G. Shapter. 2019. "Single-walled Carbon Nanotubes Enhance the Efficiency and Stability of Mesoscopic Perovskite Solar Cells". figshare. <https://hdl.handle.net/2134/25302>.

Single-Walled Carbon Nanotubes Enhance the Efficiency and Stability of Mesoscopic Perovskite Solar Cells

Munkhbayar Batmunkh,^{†,‡} Cameron J. Shearer,[†] Munkhjargal Bat-Erdene,[†] Mark J. Biggs,^{‡,§} and Joseph G. Shapter^{†}*

[†] School of Chemical and Physical Sciences, Flinders University, Bedford Park, Adelaide, South Australia 5042, Australia

[‡] School of Chemical Engineering, The University of Adelaide, Adelaide, South Australia 5005, Australia

[§] School of Science, Loughborough University, Loughborough, Leicestershire, LE11 3TU, UK

KEYWORDS

Perovskite solar cells, TiO₂ photoelectrode, carbon nanotubes, device performance, device stability

ABSTRACT: Carbon nanotubes are 1D nanocarbons with excellent properties and have been extensively used in various electronic and optoelectronic device applications including solar cells. Herein, we report a significant enhancement in the efficiency and stability of perovskite solar cells (PSCs) by employing single-walled carbon nanotubes (SWCNTs) in the mesoporous photoelectrode. It was found that SWCNTs provide both rapid electron transfer and advantageously shifts the conduction band minimum of the TiO_2 photoelectrode and thus enhances all photovoltaic parameters of PSCs. The TiO_2 -SWCNTs photoelectrode based PSC device exhibited a power conversion efficiency (PCE) of up to 16.11%, while the device fabricated without SWCNTs displayed an efficiency of 13.53%. More importantly, we found that the SWCNTs in the TiO_2 nanoparticles (TiO_2 NPs) based photoelectrode suppress the hysteresis behavior and significantly enhance both the light and long-term storage-stability of the PSC devices. The present work provides important guidance for future investigations in utilizing carbonaceous materials for solar cells.

1. INTRODUCTION

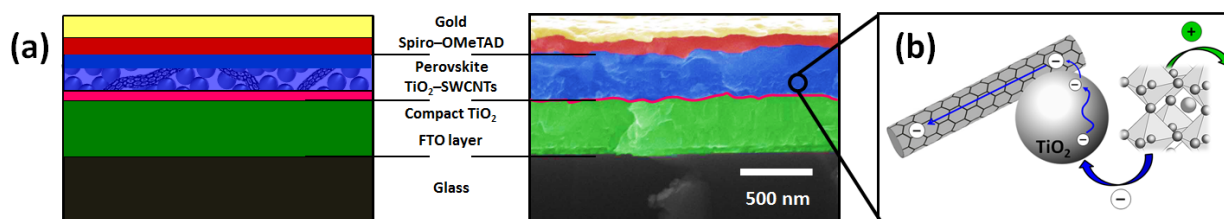
Since the pioneering work on organometal halide perovskite (ABX_3 , A = organic cation, B = metal cation, and X = halide) based photovoltaic (PV) cells was reported in 2009,¹ perovskite solar cells (PSCs) have attracted significant attention and are now sitting in the spotlight as a promising technology for renewable energy production.²⁻⁴ This emerging PV system, in comparison to traditional silicon solar cells, promises to be less expensive, lighter, more flexible and portable.⁵⁻⁹ More importantly, the power conversion efficiency (PCE) of these PV devices has reached a certified value of 22.1% and is approaching that of the conventional silicon solar cells.¹⁰⁻¹²

High PCEs have been mainly achieved using mesoscopic structured PSCs.¹²⁻¹⁴ The heart of the mesoscopic PSC system is a semiconducting oxide electron transporting material (ETM) that collects photogenerated electrons from the perovskite light absorber and injects them into an external circuit. Typically, nanocrystalline TiO₂ particles are used as the ETM.^{15, 16} However, the electron transport in the disordered TiO₂ nanocrystallite network involves a random transit path and numerous grain boundaries increasing the rate of charge recombination and thus limiting device efficiency.¹⁷⁻¹⁹ Therefore, designing photoelectrodes with improved charge transport pathways is expected to enhance the efficiency of PSCs.

A variety of strategies have been developed to improve the electron transport properties of PSC photoelectrodes.²⁰⁻²³ In particular, graphene and its derivatives for use in the photoelectrodes of PSCs have recently attracted increasing attention due to graphene's availability, high conductivity and suitable energy levels.^{19, 24, 25} Although PSCs based on photoelectrodes with various graphene derivatives incorporated have shown enhancement in the performance compared to their control devices, the obtained efficiencies are still limited probably due to the structural defects of the graphene sheets created during the production process. In this regard, carbon nanotubes (CNTs), particularly single-walled (SWCNTs), are expected to exhibit significant enhancement in the PCE of PSCs because of their unique structure and excellent properties. It is worth noting that in dye-sensitized solar cell (DSSC) systems, CNTs have been shown to be more effective in enhancing the PCE than other carbon materials.^{26, 27} Despite this great promise, there has been no effort focused on employing CNTs in nanocrystalline TiO₂ photoelectrodes for PSCs.

Herein we introduce SWCNTs into the nanocrystalline TiO₂ porous layers to fabricate PSC devices illustrated in **Scheme 1**. The incorporation of SWCNTs into the PSC photoelectrodes

was found to be far more effective than the other types of nanocarbon materials including graphene and its derivatives. By finding an optimal loading of SWCNTs, the PSC device fabricated based on TiO₂ NPs-SWCNTs hybrid photoelectrode achieved a maximum PCE of 16.11%, which was significantly higher than that (13.53%) of the TiO₂ NPs based control cells. In addition to this impressive PCE, we found that the use of SWCNTs in the nanocrystalline TiO₂ photoelectrodes reduces the anomalous hysteresis behavior and considerably enhances the light- and long-term storage-stability of the PSC devices.



Scheme 1. (a) Schematic representation (left) and cross sectional SEM image (right) of the TiO₂ NPs-SWCNTs photoelectrode based PSC device. (b) Schematic illustration of the improved charge transport process in the TiO₂ NPs-SWCNTs nanocomposite.

2. EXPERIMENTAL SECTION

2.1. Materials

All chemicals and reagents were purchased from Sigma-Aldrich, unless otherwise specified. (2,2',7,7'-tetrakis-(*N,N*-di-*p*-methoxyphenylamine)-9,9'-spirobifluorene) (Spiro-OMeTAD) was obtained from Solaronix, Switzerland. A fluorine-doped tin oxide (FTO) coated glass electrode, transparent titania (TiO₂) paste (18NR-T), methylammonium iodide (CH₃NH₃I), tris(1-(pyridin-2-yl)-1*H*-pyrazol)cobalt(III)tris(hexafluorophosphate) (FK102 Co(III) PF₆) salt were purchased

from Dyesol, Australia. Arc-discharge SWCNTs (P3-SWNT) were purchased from Carbon Solution Inc., Riverside, CA, USA.

2.2. Preparation of TiO₂ NPs-SWCNTs nanocomposites

The stock solution (aqueous) of SWCNTs with 1 mg mL⁻¹ concentration was prepared according to the previous reported method.²⁸ Briefly, SWCNTs (10 mg, P3-SWNT) were bath sonicated for 1 h in aqueous Triton-X 100 (10 mL, 1% v/v). On the other hand, the commercially available TiO₂ paste (Dyesol, 18NR-T) was diluted in ethanol (1:5.5 w/w). In order to prepare the TiO₂ NPs-SWCNTs, an appropriate volume of the CNTs stock solution was added into the diluted TiO₂ dispersion. The concentration of SWCNTs in the nanocomposite was adjusted by changing the volume of CNT solution.

2.3. Device Fabrication

FTO-coated glass substrates were first etched using 2M HCl and Zn powder. Then the etched FTO substrates were cleaned with a detergent (Pyroneg) and washed with acetone, ethanol, and DI water using an ultrasonication for 10 min each. A 50 nm TiO₂ compact layer was deposited onto the FTO substrate via spin coating 0.15 M titanium diisopropoxide bis(acetylacetonate) (75 wt% in isopropanol, Aldrich) in 1-butanol. The spin coating was carried out for 25 s at 2000 rpm with a ramp of 1000 rpm s⁻¹. After each spin coating, the electrodes were dried by heating at 150 °C for 15 min in air. Upon cooling to room temperature, the mesoporous TiO₂ layer without and/or with SWCNTs was deposited onto the compact TiO₂ film by spin coating the previously

prepared (diluted) TiO₂ solution with different amounts of SWCNTs for 25 s at 4000 rpm with a ramp of 2000 rpm s⁻¹. The photoelectrodes were then heated gradually in air at 125 °C for 5 min, 325 °C for 5 min, 375 °C for 15 min, and 450 °C for 1 h. After cooling to room temperature, the films were immersed in a 20 mM aqueous TiCl₄ solution at 90°C for 15 min and the resulting films were again annealed at 450 °C for 1 h. After cooling to ~120 °C, the films were transferred into a nitrogen-filled glove box for the deposition of perovskite layer, hole transport layer (HTL) and Au electrode.

PbI₂ (0.507 g) and CH₃NH₃I (0.175 g) were mixed in anhydrous dimethylsulfoxide (DMSO, 1 mL) to prepare the perovskite precursor solution. The deposition of the perovskite layer was performed according to a previously established spin coating method.^{29, 30} The spin coating recipe includes two steps, first 1000 rpm for 10 s with a ramp of 250 rpm s⁻¹, then 5000 rpm for 30 s with a ramp of 2000 rpm s⁻¹. ~12 s before the end of the spin-coating program, anhydrous chlorobenzene (120 µL) was gently dropped on the centre of spinning substrate. The films were then heated at 100 °C for 1h in a glovebox.

After drying the perovskite coated films in the glove box, the hole transporting material (HTM) (50 µL) was deposited onto the perovskite layer by spin coating for 20 s at 4000 rpm with a ramp of 2000 rpm s⁻¹. The HTM was prepared by dissolving 28.9 mg Spiro-OMeTAD, 11.5 µL 4-*tert*-butylpyridine (tBP), 7.0 µL of a stock solution of 520 mg mL⁻¹ lithium bis(trifluoromethylsulphonyl)imide (Li-TFSI) in acetonitrile and 9.0 µL of a stock solution of 100 mg mL⁻¹ FK102 Co(III) PF₆ salt in acetonitrile, in 400 µL chlorobenzene. After the HTM deposition, the films were stored overnight in a dry air desiccator. Finally, 50 nm gold electrodes were thermally evaporated (Angstrom Engineering Covap) at a rate of 1 Å s⁻¹ under high vacuum through a shadow mask.

2.4. Measurement and Characterization

Scanning electron microscopy (SEM) images were obtained using an Inspect F50 SEM (FEI) with accelerating voltage of 20 kV. Raman confocal spectroscopy and spectral mapping were completed using a Witec Alpha 300RS with a 40 x objective and 532 nm laser excitation. Raman single spectra were acquired with integration times of 5 s and 3 accumulations. The Raman spectral image was obtained by collecting a series of 100 x 100 single spectra (0.5 s integration per spectrum) over an area of 20 x 20 μm . Electrochemical impedance spectroscopy (EIS) was carried out with an Autolab PGSTAT128N on the fabricated PSC devices. Analysis was completed under light at 0.3 V bias with 10 mV modulation over the frequency range of 100000 – 0.1 Hz. Measurements were taken under illumination from an optic fibre light source (Dolan-Jenner Fiber-Lite 190-1) at $\sim 35 \text{ mW cm}^{-2}$, which was measured with a light meter (Newport Power Meter, model 1815-C). Sheet resistance measurements were performed on the same films using a four point probe technique (KeithLink Technology Co., Ltd. Taiwan). Steady-state photoluminescence (PL) measurements were performed with a Cary Eclipse Fluorescence Spectrophotometer (Agilent Technologies), using an excitation wavelength of 445 nm.

The photocurrent–voltage (J – V) characteristics were analysed using a Keithley 2400 SMU instrument and recorded using a custom LabView Virtual Instrument program. A standard Silicon test cell with NIST-traceable certification was used to calibrate the power density at 100 mW cm^{-2} at the sample plane of the collimated a 150W xenon-arc light source (Newport), which was passed through an AM 1.5G filter. The scan rate and delay time are 200 mV s^{-1} and 30 ms, respectively. The active area of the devices was 0.1 cm^2 . The devices were masked with a non-reflective mask of 0.1 cm^2 and were tested in an air atmosphere without encapsulation. No

device preconditioning, such as prolonged light soaking, forward voltage biasing, or equilibration time was used. The incident-photon-to-current conversion efficiency (IPCE) spectra ranging from 300 nm to 800 nm were taken by passing chopped light from a xenon source through a monochromator and onto the devices. The light intensity of the illumination source was adjusted using a photodiode detector (silicon calibrated detector, Newport).

3. RESULTS AND DISCUSSION

SWCNTs were incorporated into the TiO₂ NPs photoelectrode by mixing solution processed SWCNTs with the TiO₂ paste prior to deposition ((SEM images of starting materials are provided in Figure S1, supporting information (SI)). **Figure 1a** shows the top view SEM image of the prepared TiO₂ NPs-SWCNTs nanocomposites. It is difficult to directly observe the well dispersed SWCNTs within the TiO₂ NP matrix. Given the low loading of the SWCNTs (0.10 % w/w), this was expected. Therefore, Raman spectral microscopy was used to determine SWCNT homogeneity in the film.

Raman spectroscopy is an important tool for analyzing carbon nanomaterials and has frequently been used to confirm the presence of nanocarbons in composites or hybrids.^{24, 26, 28} Raman spectra of the samples were collected and are plotted in Figure 1b to further confirm the existence of SWCNTs in the nanocomposite. The Raman peaks located at around 150, 398, 518 and 641 cm⁻¹ correspond to the typical modes of the anatase TiO₂.²⁴ The SWCNT spectra showed the feature peaks at 1357 and 1597 cm⁻¹, which can be assigned to the disorder-induced “D” band and the “G” band, in addition to the typical radial breathing mode (RBM) and “G” band peaks. When analyzing the composite film (blue series, Figure 1b) Raman signals

corresponding to both TiO₂ NPs and CNTs throughout the sample were observed. Confocal Raman spectral microscopy maps of the TiO₂ NPs-SWCNTs nanocomposites shown in Figure 1c illustrate the distribution of SWCNTs throughout the TiO₂ NP matrix, confirming that the existence of both TiO₂ and SWCNTs in the sample.

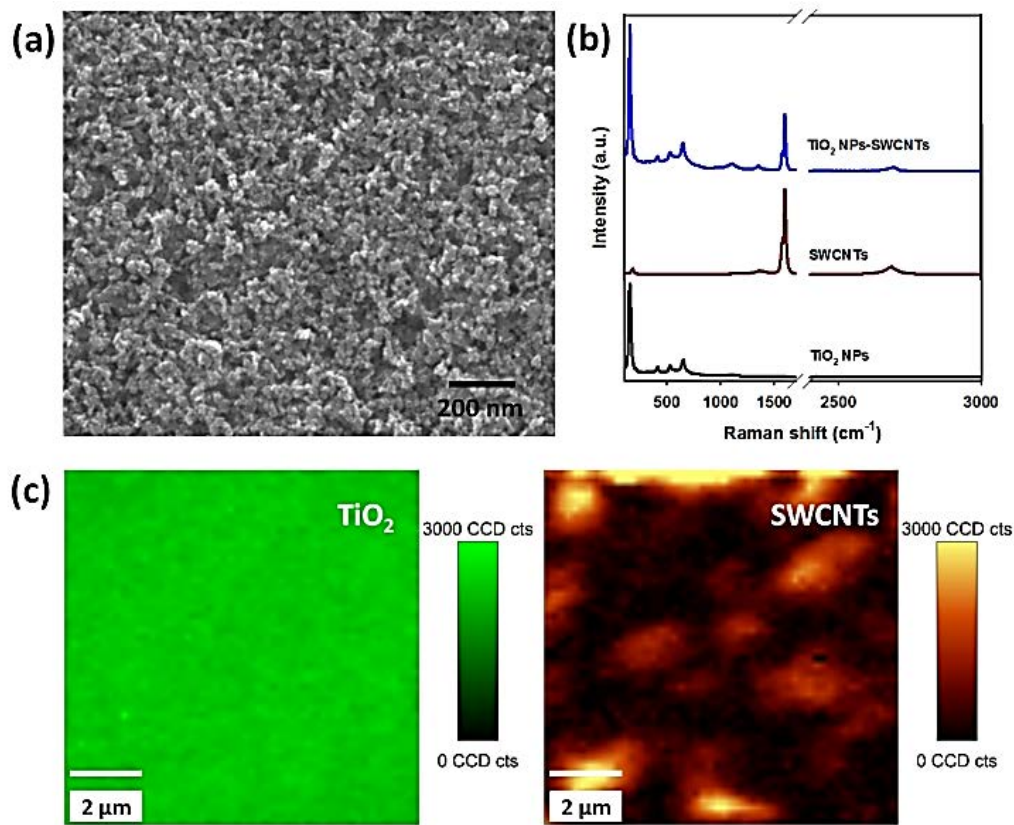


Figure 1. (a) Top-view SEM image of TiO₂ NPs-SWCNTs nanocomposite. (b) Raman spectra of TiO₂ NPs, SWCNTs and their nanocomposite. (c) Raman spectral mapping the same area (20 x 20 μm) showing distribution of TiO₂ NPs (left, green) and SWCNTs (right, orange) in the composite. The color scale represents the sum of the anatase TiO₂ and CNT related signal, respectively.

After confirming the presence of SWCNTs throughout the TiO₂ NP film, the SWCNT content was varied to determine optimal content to maximize the PCE of PSCs. Five photoelectrodes of different SWCNT contents in the composite were used from 0 wt% to 0.50 wt% to fabricate PSCs such as the representative cell illustrated in Figure S2. Our PSCs were fabricated based on CH₃NH₃PbI₃ which was deposited on TiO₂ NPs films with and without SWCNTs. The PV characteristics of these PSCs were evaluated using simulated AM1.5 sunlight with an output power of 100 mW cm⁻² and are shown in Figure S3. Detailed PV parameters of these PSCs have been summarized in **Figure 2** and **Table 1**.

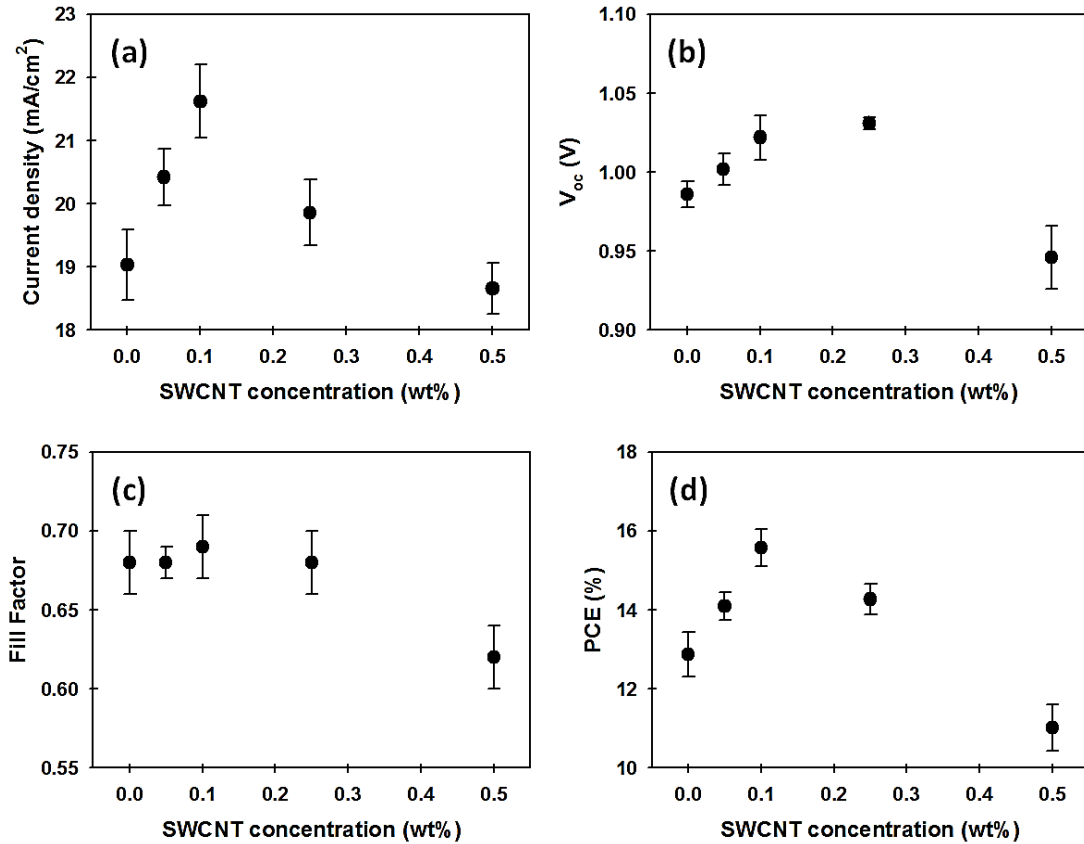


Figure 2. Plots of (a) J_{sc} , (b) V_{oc} , (c) FF and (d) PCE of the PSCs as a function of SWCNT concentration in the TiO₂ films.

Starting from the control PSCs fabricated based on TiO₂ NPs-only photoelectrodes, the average short-circuit current (J_{sc}), open-circuit voltage (V_{oc}) and fill factor (FF) are 19.03 mA cm⁻², 0.986 V and 0.68, respectively. With increasing SWCNT loading in the TiO₂ NPs photoelectrodes, both the J_{sc} and V_{oc} values of the devices increased to 21.62 mA cm⁻² and 1.022 V, respectively, peaking at 0.10 wt%, followed by a decrease with further increases in the concentration of SWCNTs. The changes in the J_{sc} values can be traced to the conductivity of the CNTs and their ambipolar nature. The improved current must result from the improved conductivity of the films initially however the addition of large amounts of CNTs introduces many junctions which will act as recombination points. These two competing factors will see a peaked dependence of current as a function of CNT loading completely in line with other observations. It is important to note that CNTs can also transport holes which will increase their lifetime in the photoelectrode and this will, at higher CNT loadings, lead to increased recombination lowering the observed current.^{27, 31} The increase in recombination rate in the photoelectrode at high loadings is also clear in the decrease in the FF at the highest loadings. There are some changes in the V_{oc} with loading. Importantly, for the lower SWCNTs loadings, the V_{oc} is higher than that observed for the electrode without the SWCNT which will be explained later. At the very highest loadings, the V_{oc} is lower than that without SWCNT likely due to increased conduction pathways that are not part of the core circuit producing current. The enhanced PV parameters of PSC devices after incorporating the optimum amount of SWCNTs in the TiO₂ NPs photoelectrodes are systematically investigated and comprehensively discussed in the following section.

Table 1. PV parameters of PSCs fabricated based on TiO₂ NP photoelectrodes with different SWCNTs loadings. Parameters of the best cells are highlighted in **bold**. The average values were calculated based on at least five devices.

Device	J_{sc} (mA cm ⁻²)	V_{oc} (V)	FF	PCE (%)
TiO ₂ NPs-only	19.485; 19.03 ± 0.56	0.988; 0.986 ± 0.008	0.70; 0.68 ± 0.02	13.53; 12.88 ± 0.56
0.05 wt% SWCNTs	20.870; 20.42 ± 0.45	1.010; 1.002 ± 0.010	0.69; 0.68 ± 0.01	14.50; 14.10 ± 0.35
0.10 wt% SWCNTs	21.964; 21.62 ± 0.58	1.041; 1.022 ± 0.014	0.70; 0.69 ± 0.02	16.11; 15.58 ± 0.47
0.25 wt% SWCNTs	20.431; 19.86 ± 0.52	1.035; 1.031 ± 0.004	0.70; 0.68 ± 0.02	14.72; 14.27 ± 0.39
0.50 wt% SWCNTs	18.975; 18.66 ± 0.41	0.956; 0.946 ± 0.020	0.64; 0.62 ± 0.02	11.64; 11.02 ± 0.59

The average efficiency of the cells increased from 12.88% (without SWCNTs) to a maximum average of 15.58% (0.10 wt%), followed by a decrease at higher content (0.25 and 0.50 wt%) of SWCNTs. The optimum PV parameters for the PSCs were achieved for the 0.10 wt% SWCNTs incorporated TiO₂ NP photoelectrode. The measured J_{sc} , V_{oc} and FF values for the best performing TiO₂ NPs-SWCNTs photoelectrode based device were 21.96 mA cm⁻², 1.041V and 0.70, respectively, yielding a PCE of 16.11%, which was significantly higher than that (13.53%) of the best control PSCs fabricated without SWCNTs in the photoelectrodes (see **Figure 3a**). Notably, this efficiency (16.11%) achieved using our SWCNTs incorporated TiO₂ NP photoelectrode is higher than other reported values of the PSC devices based on photoelectrodes

with carbonaceous content.^{19, 23-25, 32, 33} Moreover, the reproducibility of PSCs based on both TiO₂ NPs-only (control) and TiO₂ NPs-SWCNTs photoelectrodes is displayed in Figure 3b, indicating that the performances of these efficient PSCs are highly reproducible. This result confirms that the addition of SWCNTs in the photoelectrodes does not alter the reproducibility of the PSC devices.

Of the major factors affecting PCE (FF , V_{oc} , J_{sc}), the incorporation of SWCNTs increases V_{oc} and J_{sc} but does not alter FF (see Figure 2). It is important to note that although the incorporation of carbon nanomaterials such as graphene and its derivatives into the PSC photoelectrodes was found to improve the cell efficiency in previous studies, the V_{oc} in these studies have remained unchanged or decreased.^{19, 25} In contrast, in the present work, the V_{oc} values of the nanocrystalline TiO₂ photoelectrode based PSC devices increased by ~50 mV after adding SWCNTs (V_{oc} for the control device fabricated based on TiO₂ only was 0.988 V while V_{oc} for the optimum SWCNTs incorporated cell was 1.041 V). Density functional theory calculations have shown that SWCNT interaction with TiO₂ (101) raises the conduction band minimum (CBM) in comparison to the TiO₂ semiconductor.³¹ The V_{oc} in PSC devices is determined by the energy difference between the CBM of the ETM and the valence band maximum of the HTM.³⁴ This theoretical study supports our experimental observation of SWCNT incorporation into the TiO₂ photoelectrode increasing the V_{oc} of PSCs. It should be noted that despite this theoretical explanation, a considerable drop in the PV parameters of the PSCs was observed for the 0.50 wt% SWCNTs incorporated TiO₂ photoelectrode. This is probably due to the fact that SWCNT is acting as a hole transporting material, which leads to a possible charge recombination within the device.²²

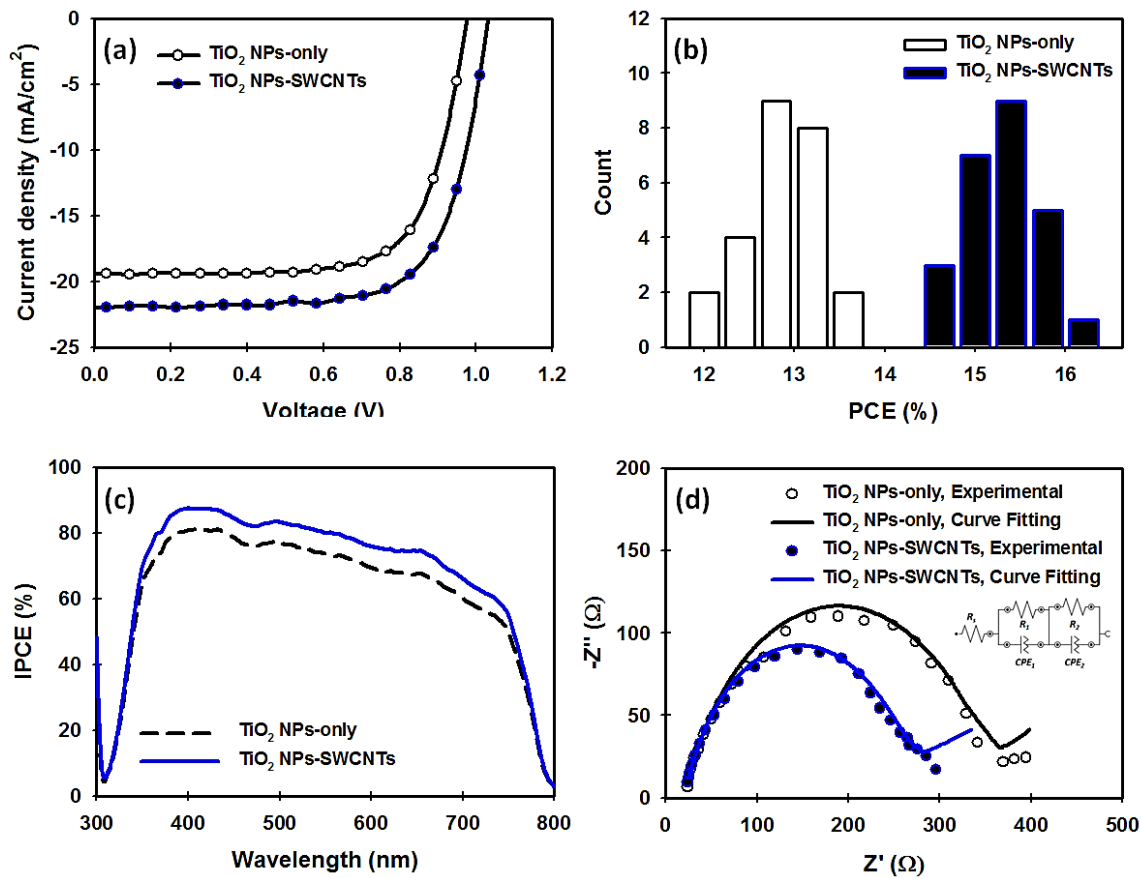


Figure 3. (a) J - V curves of the best performing PSCs fabricated with and without SWCNTs (0.10 wt%) in the photoelectrodes measured under 100 mW cm^{-2} (AM 1.5G) illumination. (b) Histogram of the PCE of devices based on TiO₂ NPs-only and TiO₂ NPs-SWCNTs photoelectrodes. (c) IPCE spectra and (d) Nyquist plots of EIS measurements of the devices measured under illumination at 0.3 V bias (V_{oc}).

With theoretical support to explain the observed increase in V_{oc} after adding SWCNTs, we sought further experimental evidence to explain the increased J_{sc} . Figure 3c displays the IPCE spectra of TiO₂ NPs-only and TiO₂ NPs-SWCNTs photoelectrodes based PSCs. The device with

SWCNT shows a clear improvement in IPCE across the entire wavelength range (from around 350 nm to 760 nm). Since the J_{sc} of the device can be determined from the IPCE spectra, the higher IPCE value with SWCNTs was expected. The integrated J_{sc} values from the IPCE spectra for the PSCs fabricated with TiO₂ NPs-only and TiO₂ NPs-SWCNTs films were 17.30 and 19.20 mA cm⁻², respectively, which are in agreement (within ±10% error) with the measured J_{sc} from the J - V characteristics of fresh devices. More importantly, the J_{sc} difference (1.90 mA cm⁻²) obtained from the integrated IPCE spectra of TiO₂ NPs-only based device and TiO₂ NPs-SWCNTs based cell was very close to that (2.30 mA cm⁻²) calculated from the J - V characteristics, confirming the relationship of the J - V curves to the IPCE spectra under AM1.5G conditions. The wavelength independent improvement of IPCE suggests the SWCNT are passively improving charge transfer.

EIS was carried out to investigate the interfacial charge transfer properties of the devices. The EIS measurements were carried out at an applied bias of 0.3V under illumination at 35 mW cm⁻² in ambient atmosphere. Figure 3d shows the Nyquist plots derived from the results of EIS spectra of TiO₂ NPs-only and TiO₂ NPs-SWCNTs photoelectrode based PSC devices, in which two RC arcs were observed. It is well established that the first arc at the higher frequency (R1) is attributed to the charge-transfer resistance (R_{ct}), while the second arc at the lower frequency (R2) is related to the recombination resistances of the fabricated PSC devices.^{31, 35} Here we focused on the R_{ct} of the devices. The SWCNTs employed PSC device exhibited lower R_{ct} (320 Ω) as compared to the control cell (376 Ω), indicating improved electron transport properties. The combination of IPCE and EIS suggest the enhanced J_{sc} by incorporating SWCNT results from improved electron transfer through the photoelectrode. This improvement in the electron

transport properties of the photoelectrodes is expected to suppress the charge recombination rate of the PSC devices.

To further investigate the reduction of the charge recombination rate at the PSC photoelectrodes in the presence of SWCNTs, dark J - V measurements of the devices were carried out to study the diode properties (see **Figure 4a**). From the dark J - V measurement, saturation-current (J_{sat}) values and ideality factor were obtained for both the TiO₂ NPs-only and TiO₂ NPs-SWCNTs photoelectrodes based PSC devices. As shown in Table S1, the J_{sat} values of the PSCs fabricated with SWCNTs in the photoelectrodes ($1.05 (\pm 0.38) \times 10^{-10}$ mA cm⁻²) were nearly five times lower than that ($5.47 (\pm 0.21) \times 10^{-10}$ mA cm⁻²) of the TiO₂ NPs-only based cells. Interestingly, the average ideality factor of TiO₂ NPs-SWCNTs photoelectrodes based PSCs is approximately 1.31 ± 0.14 , while the control devices showed average ideality factor of 1.46 ± 0.14 . We note that the ideality factors of our devices were considerably lower than those reported in recent study using graphene derivatives incorporated mesoporous TiO₂ NPs films based PSCs.²⁵ A lower J_{sat} value and an ideality value closer to 1 both indicate less charge recombination from reverse current and charge trapping is occurring in the diode.^{25, 28, 36, 37} Moreover, the measurement of sheet resistance (R_s) of the thin films (on glass substrates) was carried out using a four point probe to explore the mechanism of J_{sc} enhancement of the devices. The R_s of the TiO₂ films with SWCNTs was $1.86 \pm 0.01 \times 10^6$ Ω, which was nearly 2.5 times lower than that ($4.51 \pm 0.005 \times 10^6$ Ω) of the TiO₂ NPs-only films. This reduction in the R_s of the films is due to the high conductivity of SWCNTs that decreases the interfacial resistance between TiO₂ NPs.

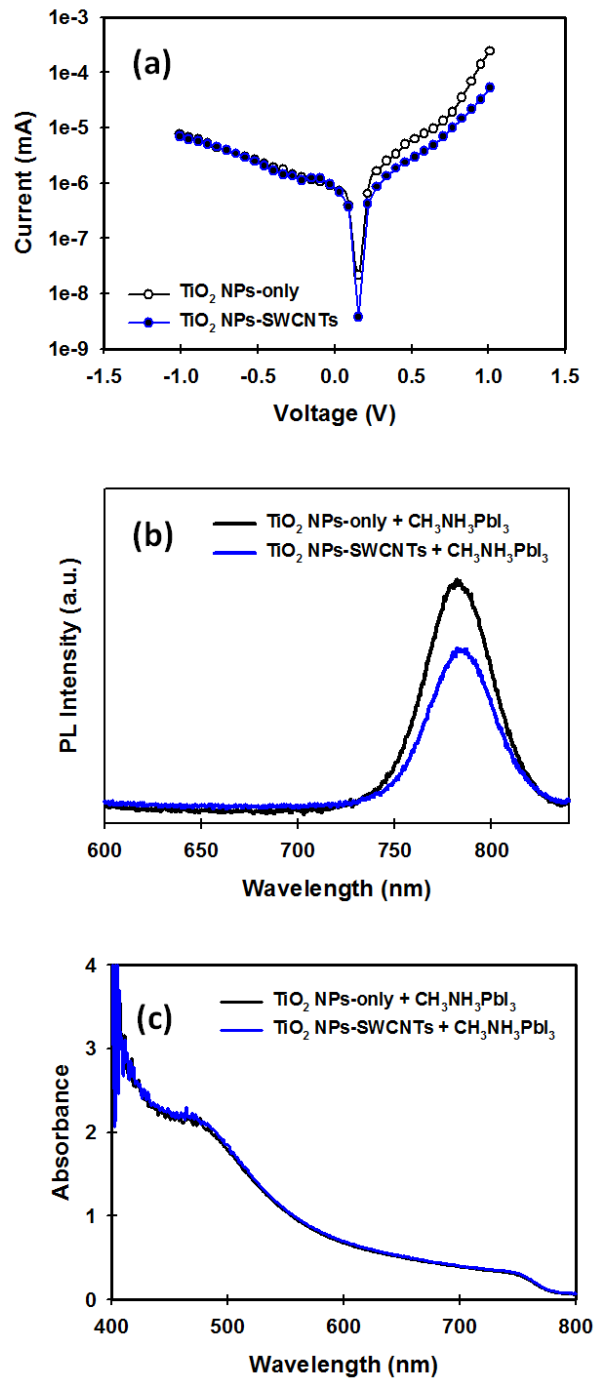


Figure 4. (a) Representative *J-V* curves of the PSCs fabricated with and without SWCNTs in the TiO_2 NPs photoelectrodes measured in dark condition in semi-logarithmic scale. (b) Steady-state PL spectra and (c) UV-vis absorption spectra of perovskite films prepared on the FTO/ TiO_2 -only and FTO/ TiO_2 -SWCNTs.

The charge dissociation and recombination processes of the PSCs fabricated based on TiO₂ NPs photoelectrodes with and without SWCNTs were studied using photoluminescence (PL) spectroscopy. The PL spectra, depicted in Figure 4b, of the perovskite films on FTO/TiO₂ NPs and FTO/TiO₂ NPs-SWCNTs were collected with an excitation wavelength of 445 nm. The PL peak at around 780 nm in Figure 4b is consistent with the previously reported emission from CH₃NH₃PbI₃.³⁸ It can be clearly seen from Figure 4b that the PL intensity of the TiO₂ NPs-SWCNTs based film is about 30% lower than that of the TiO₂ NPs-only based film. It is well known that the rapid recombination of the photogenerated electrons and/or holes leads to emission of strong PL. A lower PL emission intensity indicates a decrease in the radiative recombination and better separation of the excitons.³⁸ This shows that the SWCNTs as electron collectors and transporters can benefit the charge transfer process in the TiO₂ NPs-SWCNTs films and suppress charge recombination. In addition to the PL characteristic of only half device (FTO/ETM/perovskite) such as that reported in this study, a comprehensive investigation on the PL characteristics of full devices has been carried out by Tvingstedt and co-workers.³⁹

These results indicate that the SWCNTs incorporated TiO₂ NPs photoelectrodes based PSCs have reduced charge recombination as compared to the TiO₂ NPs-only based devices. In addition, the device fabricated with SWCNTs exhibited reduced series resistance (R_{series} , Table S1) ($77.3 \pm 7.96 \Omega$ for the cells with SWCNTs and $111 \pm 10.5 \Omega$ for the devices without SWCNTs), which further confirms the R_{ct} of the cells obtained from the EIS analysis. Moreover, we note that no difference in light absorption including the intensity of the perovskite films was observed after adding 0.10 wt% SWCNTs into the TiO₂ NPs films (Figure 4c). This indicates that the use of small amount of SWCNTs does not significantly change the crystallization of perovskite.

Widespread commercial application of PSC will not become a reality without significant improvement to stability and reduction of J - V hysteresis. We have compared the hysteresis behavior and stability of PSCs with and without SWCNTs.

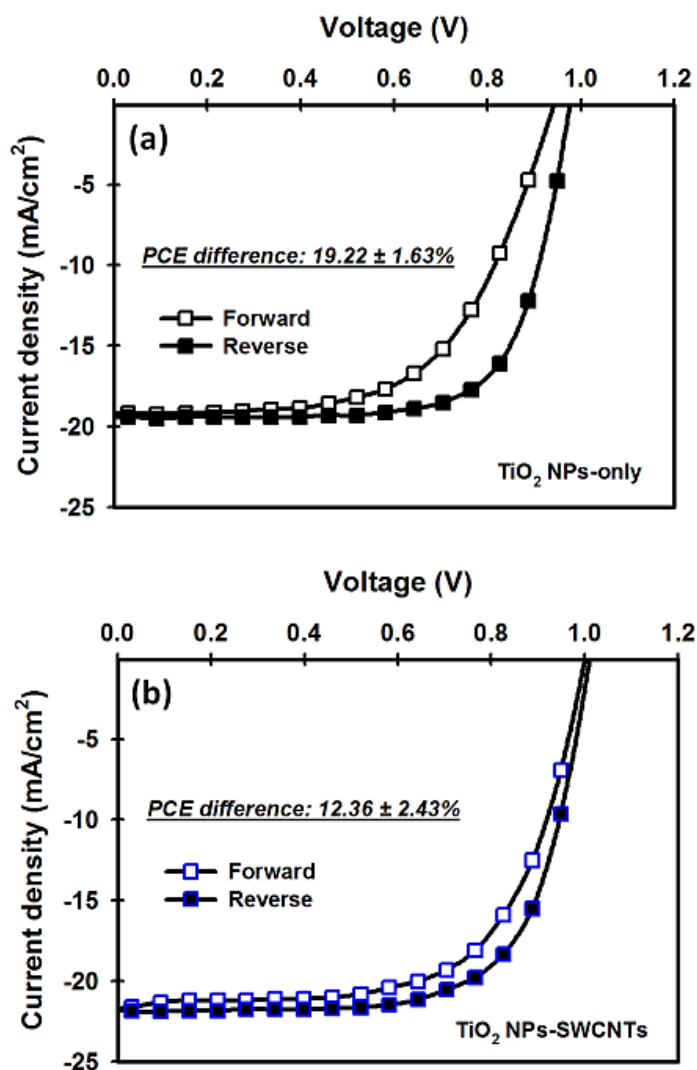


Figure 5. Representative J - V curves of the (a) TiO₂ NPs-only and (b) TiO₂ NPs-SWCNTs photoelectrode based PSCs measured with reverse and forward scans. PCE differences are calculated using Eq. 1. Standard deviations are calculated based on at least 3 devices. The scan rate was 200 mV s⁻¹.

Anomalous hysteresis behavior observed during the J - V analysis of PSCs limits their stabilized power output under working conditions and causes serious issues for the device stability and PCE accuracy.^{40, 41} J - V curves of the devices (at least 3 cells for each device structure) measured were recorded using different scan directions (reverse and forward) and the representative results are plotted in **Figure 5a** and 5b. Detailed PV parameters have been summarized in Table S2. To provide reasonable comparison, PCE difference (known as the difference factor)⁴² of the PSCs was calculated according to the following equation.

$$PCE_{difference} = \frac{PCE_{reverse} - PCE_{forward}}{PCE_{reverse}} \quad \text{Eq. (1)}$$

From the Eq. (1), a high PCE difference means the cells show large hysteresis and distortion. For the control cell without SWCNTs, the calculated average PCE difference was $19.22 \pm 1.63\%$, which was considerably higher than that ($12.36 \pm 2.43\%$) of the TiO₂ NPs-SWCNTs photoelectrode based PSC device. Therefore, it is clear that the use of SWCNTs in the nanostructured photoelectrodes significantly reduced the hysteresis behavior of the PSCs. Although the fundamental mechanism of hysteretic J - V behavior in the PSC devices is not well understood, recent theoretical and experimental studies put forward several explanations. It has been reported that an anomalous hysteresis in PSCs arises from the trap-assisted charge recombination at the interface between perovskite and ETM.^{25, 43} Therefore, the reduced hysteresis of our PSC devices fabricated with TiO₂ NPs-SWCNTs photoelectrodes may be explained by the decreased recombination at the perovskite and ETM interfaces.

Solar cell stability and lifetime is one of the most significant road blocks toward commercialization of PSCs in the quickly growing renewable electricity generation market. In

particular, $\text{CH}_3\text{NH}_3\text{PbI}_3$ based PSC devices suffer from intrinsic instability under continuous light and humid conditions, although they can exhibit remarkable performance. Here we investigated both the light- and long-term storage-stability of the PSCs with and without SWCNTs in the photoelectrodes (**Figure 6**).

The light-stability of the unencapsulated PSCs fabricated with TiO_2 NPs-only and TiO_2 NPs-SWCNTs photoelectrodes, shown in Figure 6a, was evaluated and tested by exposing cells to continuous light illumination (100 mW cm^{-2} , xenon lamp) under ambient conditions. It can be seen that the devices employing SWCNTs exhibited relatively better stability than the TiO_2 NPs-only photoelectrode based devices. For instance, the J_{sc} value of the control devices degraded by 41% after 40 min, whereas the cells fabricated with SWCNTs only degraded by ~26% of their initial J_{sc} . In our study, the PCE degradation of the devices under prolonged light soaking is mainly due to the photocurrent reduction, which is in good agreement with recent comprehensive investigations of PSC stability by Snaith's group.^{44, 45} It was reported that upon exposure of the TiO_2 to light, the holes in valence band recombine with adsorbed molecular oxygen, causing desorption and leaving positively charged deep trap sites in the TiO_2 surface. These deep trap sites then act as sinks for electrons, with recombination of the trapped electrons occurring directly with the holes in the perovskite or HTM.⁴⁵ In this regard, the SWCNTs with their excellent conductivity may be suppressed this recombination process by providing an alternative charge transport path and thus improving the device stability. Additionally it is well known that SWCNTs adsorb molecular oxygen very strongly.⁴⁶ As such, it is very likely that in the structure reported here the SWCNTs will be a sink for some of the molecular oxygen adsorbed on TiO_2 and hence decrease the production of the detrimental deep trap sites. The thermal conductivities of SWCNTs will more effectively remove heat during operation which helps stability.

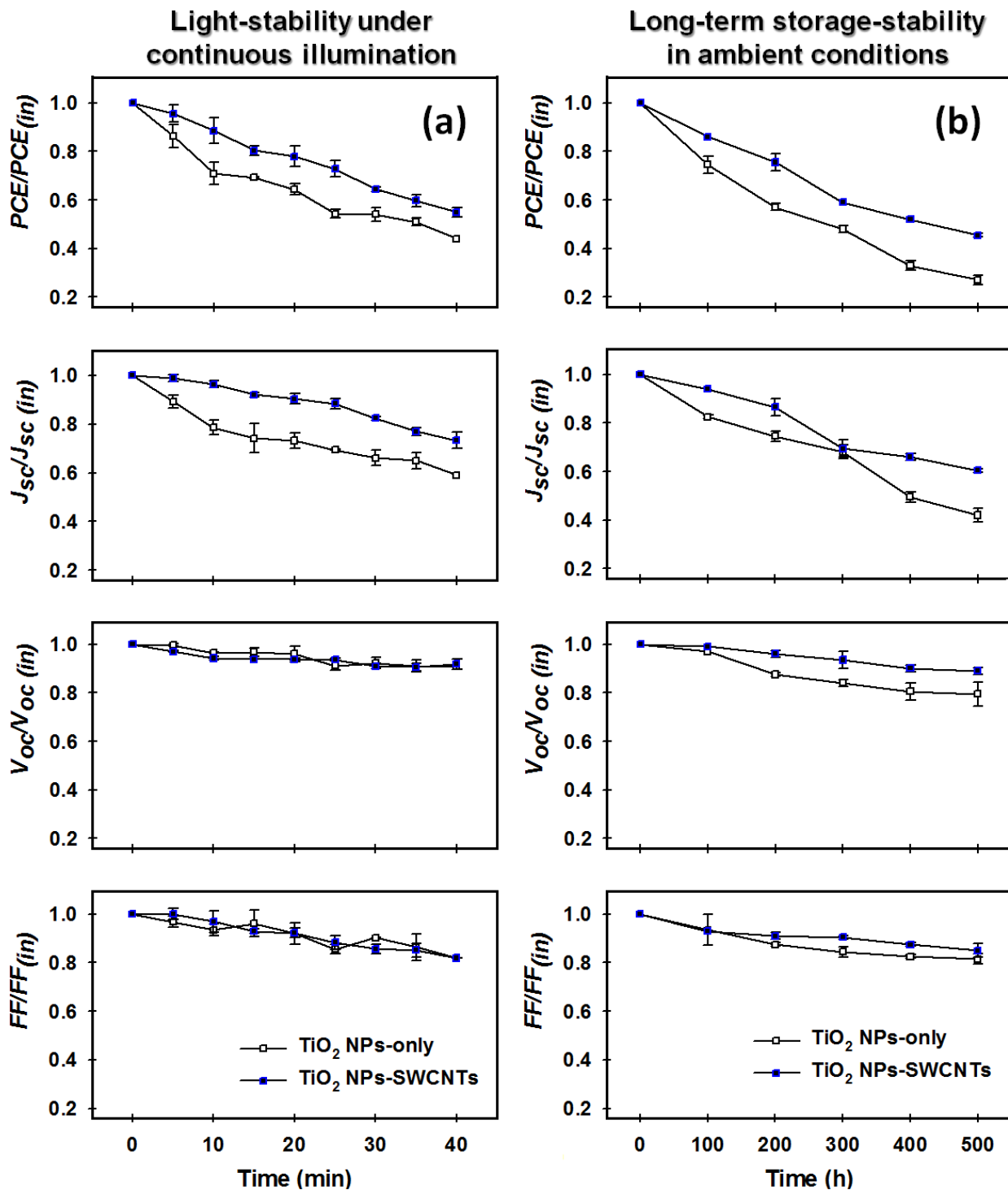


Figure 6. (a) Light and (b) long-term storage-stability of the devices fabricated with and without SWCNTs in the photoelectrodes. For the light-stability test, the cells were exposed to continuous light illumination (100 mW cm^{-2}) in ambient conditions and the data were obtained in reverse scan direction at every 5 min. For the cell storage-stability in ambient environment, the

fabricated devices were kept in the dark in ambient conditions for 500 h. The devices were not encapsulated for the stability test. In Y-axis (normalized PV parameters), $PCE_{(in)}$, $J_{sc(in)}$, $V_{oc(in)}$ and $FF_{(in)}$ represents the initial (0 hr) PV values of the devices.

Figure 6b illustrates the normalized PV parameters (J_{sc} , V_{oc} , FF and PCE) of the PSC devices fabricated with and without SWCNTs in the photoelectrodes over 500 h (3 weeks). For the stability test, the unencapsulated devices were stored in the dark in ambient conditions at a relative humidity of $>60\%$ and were tested every 100 hours. While both devices degraded, the device with SWCNTs exhibited improved stability. In particular, the devices based on TiO_2 NPs-SWCNTs photoelectrodes preserved 45.5% of the initial PCE after aging for 500 h under humid environment, whereas the PSC fabricated without SWCNTs retained only 27% of its initial performance. In order to confirm this stability improvement in the PSC performance with SWCNTs in the photoelectrode, dark J - V characteristics and EIS analysis of unencapsulated aged (~ 250 h stored in ambient conditions) devices with and without SWCNTs were investigated. It was observed from the dark J - V measurements that the ideality factor of the TiO_2 NPs-SWCNTs photoelectrode based PSC is 1.94 which was lower than that (2.23) of the control cell. In addition, the J_{sat} values of the PSCs fabricated with and without SWCNTs photoelectrodes were 1.51×10^{-7} mA cm $^{-2}$ and 1.37×10^{-6} mA cm $^{-2}$, respectively. The J_{sat} difference between TiO_2 NPs-only and TiO_2 NPs-SWCNTs films based 250 h-aged PSCs was nearly 10 times, while the difference in their fresh devices was around 5 times. This clearly confirms that the SWCNTs not only enhance the PV performances of the PSCs, but they also improve the stability of the devices in ambient conditions. This finding was further confirmed by EIS analysis of the aged PSCs. As shown in Figure S4, the SWCNTs employed PSC device

showed a reduced R_{ct} and an increased recombination resistance. In the aged devices, the R_{ct} difference between the PSCs fabricated with and without SWCNTs was around 120 Ω , while the previously measured R_{ct} difference for the freshly prepared PSC devices was only $\sim 60 \Omega$ (for both cases, SWCNTs based cells have lower R_{ct}). The higher difference in the R_{ct} of the PSCs with and without SWCNTs after aging is indicative of improved stability of the device with SWCNTs.

Moreover, much higher SWCNT loading (0.50 wt%) in the TiO₂ NPs film exhibited significantly enhanced cell stability under the same condition (relative humidity, RH > 60%) (see Figure S5), which further confirms that the employment of SWCNTs in the nanocrystalline TiO₂ NPs photoelectrodes improves the long-term storage-stability of the PSC devices. We attribute this storage-stability enhancement of the SWCNTs incorporated devices to the wettability of the photoelectrode film (see Figure S6). We believe that the hydrophilic nature of the TiO₂ film (Figure S6a) could have adsorbed some moisture before the deposition of perovskite, and the adsorbed moisture gradually degrades the perovskite over a period of time. On the other hand, the incorporation of SWCNTs in the TiO₂ film might help decrease the amount of moisture adsorbed as compared to the TiO₂-only film due to their greater hydrophobicity (Figure S6b). Clearly, lower amounts of moisture in the photoelectrode will cause a lower level of degradation of the perovskite. In addition, recently, Huang et al.⁴⁷ reported that the polar nature of the water molecules causes the decomposition of perovskite structures and results in severe morphological changes (formation of pinholes and coarsening of the crystalline surface) in humid conditions. This was revealed based on SEM analysis that densely packed large perovskite grains change into relatively small grains after long-term storage under ambient conditions. Such morphological features such as pinholes, small grains and coarse surface would be detrimental to

the direct charge transfer between perovskite and TiO₂. The TiO₂ NPs-SWCNTs interface provides better connectivity with the perovskite and hence provides extra charge carrying pathways which will somewhat mitigate the changes in the perovskite structure. Ultimately this should extend the electron lifetime in the device helping maintain performance over longer time.

Although this study clearly demonstrates that the application of SWCNTs in the PSC photoelectrodes play significant role in improving the device stability, the exact mechanism of stability improvement still remains to be explored in the future with experimental and theoretical investigations. We anticipate that further improvement in the device performance will be achieved by using chirality specific SWCNTs as it allows the precise tuning of electronic energy levels in the electrode.

4. CONCLUSION

In summary, we have produced a nanocomposite material comprising nanocrystalline TiO₂ NPs and conductive SWCNTs to prepare photoelectrodes for highly efficient PSCs. We found that the incorporation of SWCNTs into the nanocrystalline TiO₂ photoelectrodes significantly improves the electron transfer process and reduces the charge recombination rate, and thus results in the enhancement of J_{sc} . In addition, the V_{oc} value of the PSCs was found to increase after introducing SWCNTs into the PSC photoelectrode due to the suitable band energy alignment. As a result, a remarkable PCE of 16.11% was achieved using the nanocomposite photoelectrode based PSC device. Importantly, we found that the use of SWCNTs in the PSC photoelectrodes reduces the anomalous hysteretic J - V behavior, while it also improves the light- and long-term storage-

stability of the devices. Finally, our work provides clear guidance for future studies in incorporating nanocarbon materials in PV devices.

ASSOCIATED CONTENT

Supporting Information.

The following files are available free of charge.

Additional experimental results from the characterizations of both materials and devices (e.g. SEM images, PV parameters, device stability, electrical and optical characterizations) in the supporting information file.

AUTHOR INFORMATION

Corresponding Author

*joe.shapter@flinders.edu.au

Author Contributions

The manuscript was written through contributions of all authors. M. Batmunkh conceived and conducted all the research phases. J. G. Shapter and M. J. Biggs directed and supervised the research. M. Batmunkh and C. J. Shearer designed the experiments and interpreted the data. M. Bat-Erdene contributed to the preparation of the materials and their characterization. All authors discussed the results and commented on the manuscript. M. Batmunkh wrote the first draft of the paper.

Notes

The authors declare no competing financial interest.

ACKNOWLEDGMENT

Munkhbayar Batmunkh acknowledges International Postgraduate Research Scholarship (IPRS) and Australian Postgraduate Award (APA) for financial support during his study in Australia. The support of the Australian Research Council Discovery Program (DP130101714, DP150101354 and DP160101301) is gratefully acknowledged. We acknowledge the use of South Australian node of the Australian Microscopy & Microanalysis Research Facility (AMMRF) and Australian National Fabrication Facility (ANFF) at Flinders University.

REFERENCES

- (1) Kojima, A.; Teshima, K.; Shirai, Y.; Miyasaka, T., Organometal Halide Perovskites as Visible-Light Sensitizers for Photovoltaic Cells. *J. Am. Chem. Soc.* **2009**, *131*, 6050-6051.
- (2) Zuo, C.; Bolink, H. J.; Han, H.; Huang, J.; Cahen, D.; Ding, L., Advances in Perovskite Solar Cells. *Adv. Sci.* **2016**, *3*, 1500324.
- (3) Jung, H. S.; Park, N.-G., Perovskite Solar Cells: From Materials to Devices. *Small.* **2015**, *11*, 10-25.
- (4) Kazim, S.; Nazeeruddin, M. K.; Grätzel, M.; Ahmad, S., Perovskite as Light Harvester: A Game Changer in Photovoltaics. *Angew. Chem. Int. Ed.* **2014**, *53*, 2812-2824.
- (5) Tong, X.; Lin, F.; Wu, J.; Wang, Z. M., High Performance Perovskite Solar Cells. *Adv. Sci.* **2016**, *3*, 1500201.

- (6) Docampo, P.; Guldin, S.; Leijtens, T.; Noel, N. K.; Steiner, U.; Snaith, H. J., Lessons Learned: From Dye-Sensitized Solar Cells to All-Solid-State Hybrid Devices. *Adv. Mater.* **2014**, *26*, 4013-4030.
- (7) Qiu, L.; Deng, J.; Lu, X.; Yang, Z.; Peng, H., Integrating Perovskite Solar Cells into a Flexible Fiber. *Angew. Chem. Int. Ed.* **2014**, *53*, 10425-10428.
- (8) Qiu, L.; He, S.; Yang, J.; Deng, J.; Peng, H., Fiber-Shaped Perovskite Solar Cells with High Power Conversion Efficiency. *Small.* **2016**, *12*, 2419-2424.
- (9) Wei, Z.; Chen, H.; Yan, K.; Yang, S., Inkjet Printing and Instant Chemical Transformation of a CH₃NH₃PbI₃/Nanocarbon Electrode and Interface for Planar Perovskite Solar Cells. *Angew. Chem. Int. Ed.* **2014**, *53*, 13239-13243.
- (10) NREL, **2017**. http://www.nrel.gov/ncpv/images/efficiency_chart.jpg.
- (11) Zhou, H.; Chen, Q.; Li, G.; Luo, S.; Song, T.-b.; Duan, H.-S.; Hong, Z.; You, J.; Liu, Y.; Yang, Y., Interface Engineering of Highly Efficient Perovskite Solar Cells. *Science.* **2014**, *345*, 542-546.
- (12) Saliba, M.; Orlandi, S.; Matsui, T.; Aghazada, S.; Cavazzini, M.; Correa-Baena, J.-P.; Gao, P.; Scopelliti, R.; Mosconi, E.; Dahmen, K.-H.; De Angelis, F.; Abate, A.; Hagfeldt, A.; Pozzi, G.; Graetzel, M.; Nazeeruddin, M. K., A molecularly Engineered Hole-Transporting Material for Efficient Perovskite Solar Cells. *Nat. Energy.* **2016**, *1*, 15017.
- (13) Molina-Ontoria, A.; Zimmermann, I.; Garcia-Benito, I.; Gratia, P.; Roldán-Carmona, C.; Aghazada, S.; Graetzel, M.; Nazeeruddin, M. K.; Martín, N., Benzotrithiophene-Based Hole-Transporting Materials for 18.2 % Perovskite Solar Cells. *Angew. Chem. Int. Ed.* **2016**, *55*, 6270-6274.

- (14) Jeon, N. J.; Noh, J. H.; Kim, Y. C.; Yang, W. S.; Ryu, S.; Seok, S. I., Solvent Engineering for High-Performance Inorganic–Organic Hybrid Perovskite Solar Cells. *Nat. Mater.* **2014**, *13*, 897-903.
- (15) Li, X.; Tschumi, M.; Han, H.; Babkair, S. S.; Alzubaydi, R. A.; Ansari, A. A.; Habib, S. S.; Nazeeruddin, M. K.; Zakeeruddin, S. M.; Grätzel, M., Outdoor Performance and Stability under Elevated Temperatures and Long-Term Light Soaking of Triple-Layer Mesoporous Perovskite Photovoltaics. *Energy Technol.* **2015**, *3*, 551-555.
- (16) Matas Adams, A.; Marin-Beloqui, J. M.; Stoica, G.; Palomares, E., The Influence of the Mesoporous TiO₂ Scaffold on the Performance of Methylammonium Lead Iodide (MAPI) Perovskite Solar Cells: Charge Injection, Charge Recombination and Solar Cell Efficiency Relationship. *J. Mater. Chem. A* **2015**, *3*, 22154-22161.
- (17) Xing, G.; Mathews, N.; Sun, S.; Lim, S. S.; Lam, Y. M.; Grätzel, M.; Mhaisalkar, S.; Sum, T. C., Long-Range Balanced Electron- and Hole-Transport Lengths in Organic-Inorganic CH₃NH₃PbI₃. *Science*. **2013**, *342*, 344-347.
- (18) Batmunkh, M.; Biggs, M. J.; Shapter, J. G., Carbonaceous Dye-Sensitized Solar Cell Photoelectrodes. *Adv. Sci.* **2015**, *2*, 1400025.
- (19) Zhu, Z.; Ma, J.; Wang, Z.; Mu, C.; Fan, Z.; Du, L.; Bai, Y.; Fan, L.; Yan, H.; Phillips, D. L.; Yang, S., Efficiency Enhancement of Perovskite Solar Cells through Fast Electron Extraction: The Role of Graphene Quantum Dots. *J. Am. Chem. Soc.* **2014**, *136*, 3760-3763.
- (20) Saliba, M.; Zhang, W.; Burlakov, V. M.; Stranks, S. D.; Sun, Y.; Ball, J. M.; Johnston, M. B.; Goriely, A.; Wiesner, U.; Snaith, H. J., Plasmonic-Induced Photon Recycling in Metal Halide Perovskite Solar Cells. *Adv. Funct. Mater.* **2015**, *25*, 5038-5046.

- (21) Yang, G.; Tao, H.; Qin, P.; Ke, W.; Fang, G., Recent Progress in Electron Transport Layers for Efficient Perovskite Solar Cells. *J. Mater. Chem. A*. **2016**, *4*, 3970-3990.
- (22) Batmunkh, M.; Shearer, C. J.; Biggs, M. J.; Shapter, J. G., Nanocarbons For Mesoscopic Perovskite Solar Cells. *J. Mater. Chem. A*. **2015**, *3*, 9020-9031.
- (23) Wang, J. T.-W.; Ball, J. M.; Barea, E. M.; Abate, A.; Alexander-Webber, J. A.; Huang, J.; Saliba, M.; Mora-Sero, I.; Bisquert, J.; Snaith, H. J.; Nicholas, R. J., Low-Temperature Processed Electron Collection Layers of Graphene/TiO₂ Nanocomposites in Thin Film Perovskite Solar Cells. *Nano Lett.* **2014**, *14*, 724-730.
- (24) Han, G. S.; Song, Y. H.; Jin, Y. U.; Lee, J.-W.; Park, N.-G.; Kang, B. K.; Lee, J.-K.; Cho, I. S.; Yoon, D. H.; Jung, H. S., Reduced Graphene Oxide/Mesoporous TiO₂ Nanocomposite Based Perovskite Solar Cells. *ACS Appl. Mater. Interfaces*. **2015**, *7*, 23521-23526.
- (25) Agresti, A.; Pescetelli, S.; Cinà, L.; Konios, D.; Kakavelakis, G.; Kymakis, E.; Carlo, A. D., Efficiency and Stability Enhancement in Perovskite Solar Cells by Inserting Lithium-Neutralized Graphene Oxide as Electron Transporting Layer. *Adv. Funct. Mater.* **2016**, *26*, 2686-2694.
- (26) Dang, X.; Yi, H.; Ham, M.-H.; Qi, J.; Yun, D. S.; Ladewski, R.; Strano, M. S.; Hammond, P. T.; Belcher, A. M., Virus-Templated Self-Assembled Single-Walled Carbon Nanotubes for Highly Efficient Electron Collection in Photovoltaic Devices. *Nat. Nanotechnol.* **2011**, *6*, 377-384.
- (27) Batmunkh, M.; Biggs, M. J.; Shapter, J. G., Carbon Nanotubes for Dye-Sensitized Solar Cells. *Small*. **2015**, *11*, 2963-2989.

- (28) Macdonald, T. J.; Tune, D. D.; Dewi, M. R.; Gibson, C. T.; Shapter, J. G.; Nann, T., A TiO₂ Nanofiber–Carbon Nanotube-Composite Photoanode for Improved Efficiency in Dye-Sensitized Solar Cells. *ChemSusChem*. **2015**, *8*, 3396-3400.
- (29) Xiao, M.; Huang, F.; Huang, W.; Dkhissi, Y.; Zhu, Y.; Etheridge, J.; Gray-Weale, A.; Bach, U.; Cheng, Y.-B.; Spiccia, L., A Fast Deposition-Crystallization Procedure for Highly Efficient Lead Iodide Perovskite Thin-Film Solar Cells. *Angew. Chem. Int. Ed.* **2014**, *126*, 10056-10061.
- (30) Rakstys, K.; Abate, A.; Dar, M. I.; Gao, P.; Jankauskas, V.; Jacopin, G.; Kamarauskas, E.; Kazim, S.; Ahmad, S.; Grätzel, M.; Nazeeruddin, M. K., Triazatruxene-Based Hole Transporting Materials for Highly Efficient Perovskite Solar Cells. *J. Am. Chem. Soc.* **2015**, *137*, 16172-16178.
- (31) Batmunkh, M.; Macdonald, T. J.; Shearer, C. J.; Bat-Erdene, M.; Wang, Y.; Biggs, M. J.; Nann, T.; Shapter, J. G., Carbon Nanotubes in TiO₂ Nanofiber Photoelectrodes for High Performance Perovskite Solar Cells. *Adv. Sci.* **2017**, *4*, 1600504.
- (32) Tavakoli, M. M.; Tavakoli, R.; Nourbakhsh, Z.; Waleed, A.; Virk, U. S.; Fan, Z., High Efficiency and Stable Perovskite Solar Cell Using ZnO/rGO QDs as an Electron Transfer Layer. *Adv. Mater. Interfaces.* **2016**, *3*, 1500790.
- (33) Abrusci, A.; Stranks, S. D.; Docampo, P.; Yip, H.-L.; Jen, A. K. Y.; Snaith, H. J., High-Performance Perovskite-Polymer Hybrid Solar Cells via Electronic Coupling with Fullerene Monolayers. *Nano Lett.* **2013**, *13*, 3124-3128.
- (34) Giordano, F.; Abate, A.; Correa Baena, J. P.; Saliba, M.; Matsui, T.; Im, S. H.; Zakeeruddin, S. M.; Nazeeruddin, M. K.; Hagfeldt, A.; Graetzel, M., Enhanced Electronic

Properties in Mesoporous TiO₂ via Lithium Doping For High-Efficiency Perovskite Solar Cells. *Nat. Commun.* **2016**, *7*, 10379.

(35) Li, J.-F.; Zhang, Z.-L.; Gao, H.-P.; Zhang, Y.; Mao, Y.-L., Effect of Solvents on the Growth of TiO₂ Nanorods and Their Perovskite Solar Cells. *J. Mater. Chem. A.* **2015**, *3*, 19476-19482.

(36) Cuevas, A., The Recombination Parameter J₀. *Energy Procedia.* **2014**, *55*, 53-62.

(37) Shockley, W.; Read, W. T., Statistics of the Recombinations of Holes and Electrons. *Phys. Rev.* **1952**, *87*, 835-842.

(38) He, M.; Chen, Y.; Liu, H.; Wang, J.; Fang, X.; Liang, Z., Chemical Decoration of CH₃NH₃PbI₃ Perovskites with Graphene Oxides for Photodetector Applications. *Chem. Commun.* **2015**, *51*, 9659-9661.

(39) Tvingstedt, K.; Malinkiewicz, O.; Baumann, A.; Deibel, C.; Snaith, H. J.; Dyakonov, V.; Bolink, H. J., Radiative Efficiency of Lead Iodide Based Perovskite Solar Cells. *Sci. Rep.* **2014**, *4*, 6071.

(40) Chen, B.; Yang, M.; Priya, S.; Zhu, K., Origin of J–V Hysteresis in Perovskite Solar Cells. *J. Phys. Chem. Lett.* **2016**, *7*, 905-917.

(41) Hashmi, S. G.; Martineau, D.; Li, X.; Ozkan, M.; Tiihonen, A.; Dar, M. I.; Sarikka, T.; Zakeeruddin, S. M.; Paltakari, J.; Lund, P. D.; Grätzel, M., Air Processed Inkjet Infiltrated Carbon Based Printed Perovskite Solar Cells with High Stability and Reproducibility. *Adv. Mater. Technol.* **2017**, *2*, 1600183.

(42) Wei, Z.; Chen, H.; Yan, K.; Zheng, X.; Yang, S., Hysteresis-Free Multi-Walled Carbon Nanotube-Based Perovskite Solar Cells with a High Fill Factor. *J. Mater. Chem. A.* **2015**, *3*, 24226-24231.

- (43) Van Reenen, S.; Kemerink, M.; Snaith, H. J., Modeling Anomalous Hysteresis in Perovskite Solar Cells. *J. Phys. Chem. Lett.* **2015**, *6*, 3808-3814.
- (44) Leijtens, T.; Eperon, G. E.; Pathak, S.; Abate, A.; Lee, M. M.; Snaith, H. J., Overcoming Ultraviolet Light Instability of Sensitized TiO₂ with Meso-Superstructured Organometal Tri-Halide Perovskite Solar Cells. *Nat. Commun.* **2013**, *4*, 2885.
- (45) Wojciechowski, K.; Leijtens, T.; Siprova, S.; Schlueter, C.; Hörantner, M. T.; Wang, J. T.-W.; Li, C.-Z.; Jen, A. K. Y.; Lee, T.-L.; Snaith, H. J., C₆₀ as an Efficient n-Type Compact Layer in Perovskite Solar Cells. *J. Phys. Chem. Lett.* **2015**, *6*, 2399-2405.
- (46) Collins, P. G.; Bradley, K.; Ishigami, M.; Zettl, A., Extreme Oxygen Sensitivity of Electronic Properties of Carbon Nanotubes. *Science*. **2000**, *287*, 1801-1804.
- (47) Huang, W.; Manser, J. S.; Kamat, P. V.; Ptasinska, S., Evolution of Chemical Composition, Morphology, and Photovoltaic Efficiency of CH₃NH₃PbI₃ Perovskite under Ambient Conditions. *Chem. Mater.* **2016**, *28*, 303-311.

TABLE OF CONTENTS

